



## ISTITUTO NAZIONALE DI RICERCA METROLOGICA Repository Istituzionale

E-beam evaporated ZnO thin films: Fabrication and characterization as UV detector

This is the author's submitted version of the contribution published as:

*Original*

E-beam evaporated ZnO thin films: Fabrication and characterization as UV detector / Portesi, Chiara; Lolli, L; Taralli, Emanuele; Rajteri, Mauro; Monticone, Eugenio. - In: THE EUROPEAN PHYSICAL JOURNAL PLUS. - ISSN 2190-5444. - 130:3(2015). [10.1140/epjp/i2015-15045-1]

*Availability:*

This version is available at: 11696/30230 since: 2021-03-08T19:27:02Z

*Publisher:*

Springer

*Published*

DOI:10.1140/epjp/i2015-15045-1

*Terms of use:*

This article is made available under terms and conditions as specified in the corresponding bibliographic description in the repository

*Publisher copyright*

SPRINGER

Copyright © Springer. The final publication is available at [link.springer.com](https://link.springer.com)

(Article begins on next page)

## E- beam evaporated ZnO thin films: fabrication and characterization as UV detector

C. Portesi\*, L. Lolli, E. Taralli, M. Rajteri, and E. Monticone

Istituto Nazionale di ricerca Metrologica INRIM, Strada delle Cacce 91,  
10135-Torino, Italy

\* Corresponding author: [c.portesi@inrim.it](mailto:c.portesi@inrim.it), +390113919414

### Abstract

In the present paper, fabrication and structural, optical and electrical characterization of ZnO thin films grown by electron gun technique are reported and the performances of a prototype of UV photodetector based on them are illustrated. ZnO thin films, fabricated on sapphire by e-beam evaporation followed by a two-steps ex-situ treatment (annealing and oxidation), are polycrystalline, with a smooth surface and show very good visible transparency and an energy gap of 3.2 eV. Preliminary results on fabrication and characterization of an UV detector are reported. The Al interdigitated contacts show a Schottky behavior, which is strongly desired in perspective of applications since it has many advantages in the aspects of high quantum efficiency, response time, low dark current, high UV/visible contrast and possible zero-bias operation.

**Keywords** ZnO; UV photodetectors; semiconductor devices; thin films

### 1. Introduction

Zinc oxide (ZnO) has attracted great interest in the scientific community because of its possible applications in ultraviolet (UV) optoelectronic field, thanks to its large excitation binding energy

(60 meV) and its wide band gap (3.37 eV) [1]. UV sensors [2] are important from the application point of view which includes, among others, space communications, bio-medical instrumentation, high temperature plasma research. During the past few years, ZnO based photodetectors, inclusive of photoconductors, metal-semiconductor-metal (MSM) photodetectors, Schottky and p-n junctions photodiodes have been largely studied. In particular, ZnO-based UV photodetectors show good responsivity, high UV/visible contrast ratio, relatively high speed and low noise characteristics. Up to now, it has been proved that high quality ZnO thin films can be grown by thermal evaporation [3, 4], molecular beam epitaxy [5-10], magnetron sputtering [11, 12], pulsed laser deposition [13, 14], spray pyrolysis [15, 16], metal organic chemical vapor deposition [17], sol gel process [18], and filtered cathodic vacuum arc [19]. By means of these methods, thin films on several substrates can be grown, such as silicon, glass, and sapphire. In the last decades, many efforts have been made to achieve good ZnO thin films on c-plane sapphire substrates, both because its oxygen sublattice has the hexagonal symmetry of ZnO and because high quality and relatively low cost  $\text{Al}_2\text{O}_3$  wafers are commercially available. In order to fabricate a ZnO UV photodetector, the ZnO thin films properties that must be optimized are good crystallinity, low surface roughness, high purity, good homogeneity on large areas, reproducibility and stability. In the choice of the fabrication technique among all those mentioned above, it should be taken in to account the possibility of fabricating ZnO thin film at relatively low temperatures and by a cheap procedure. To the best of the authors' knowledge, there are limited reports on the fabrication of high performance ZnO based UV detectors by electron gun.

In the present paper, fabrication and structural, optical and electrical characterization of ZnO thin films grown by e-gun are reported. Electron gun evaporation technique, followed by a two-steps ex-situ post-treatment (annealing and oxidation), has been used because it allows the growth of high quality ZnO films. X-Ray diffraction (XRD), Scanning Electron Microscope (SEM) and Atomic Force Microscope (AFM) analysis have been carried out to characterize the morphological and structural properties of the samples. By Spectroscopic Ellipsometry, the optical constants of the

ZnO films grown by this technique have been obtained together with an estimation of roughness. The photodetector has been fabricated by traditional optical lithography and standard lift-off process for defining both the active area and the interdigitated electrodes. The device has been characterized in terms of responsivity, in air and in vacuum, and response time.

## 1. Experimental details

ZnO thin films with thickness ranging from 100 nm to 300 nm have been deposited by electron gun technique, starting from commercial powder (Alfa Aesar 99.999% ), on sapphire substrates (either 1102 or 0001 oriented). Sapphire is transparent to UV radiation, therefore it allows its backside illumination during the characterization and the measurement of the device. This would remove the problem related to the active area reduction due to the interdigitated contacts. During the deposition, the distance from the source to the substrate was 15 cm. The vacuum before evaporation was  $10^{-4}$  Pa and during evaporation, regardless of the substrate temperature, was about  $9 \times 10^{-3}$  Pa. The deposition rate was about 2-3 nm/sec. After deposition at room temperature (RT), films were dark gray. This color may be due to the oxygen deficiency and a large number of defects. Therefore, these films were annealed in air at temperature of 500°C for 30 minutes. After annealing, films were transparent in the visible range, according to literature data [20]. Other substrates temperatures ( $T_s$ ) during deposition ( $T_s$  from 100 to 300 °C) and annealing conditions ( $T_{ann}$  of 600°C for 45') were experimented.

To obtain electrically measurable samples, Al interdigitated contacts have been defined on patterned ZnO. Zinc oxide rectangular areas have been structured by optical lithography and removal of the unwanted material by chemical etching using an acid solution (HF 25% v/v in water). The ZnO area was 120  $\mu$ m wide and 530  $\mu$ m long. An alternative method for obtaining structured ZnO samples has been also experimented, based on the lift-off technique, followed by the thermal treatment described above (500°C for 30 minutes). Interdigitated metal electrodes have been then defined by

lift-off technique (optical lithography and deposition of 150 nm of metal) and are 154  $\mu\text{m}$  long, 8  $\mu\text{m}$  wide, with an inter-electrodes spacing of 15  $\mu\text{m}$ .

Just before the definition of the interdigitated contacts, the structured ZnO samples are chemically oxidized using a boiling hydrogen peroxide solution (30% v/v in water) in which they are dipped for 1 minute. According to literature [21, 22], this treatment is found an effective method to suppress the chemisorption effect and the oxygen vacancy in nanometer-thick ZnO films.

The XRD spectra of ZnO thin films (as-grown and after annealing) were recorded with an X'pert PRO PMD Panalytical diffractometer using Cu  $K\alpha$  radiation and grazing angle thin film configuration that keeps constant at  $\omega = 5^\circ$  the incident beam while the  $2\theta$  ranges between  $25^\circ$  and  $45^\circ$ .

Morphological properties have been investigated by Atomic Force Microscopy (DME instruments) in ScanAsyst mode.

SEM images have been collected by Inspect-F Scanning Electron Microscope (FEI Instruments).

The optical characterization has been performed in ambient by using a Vertical-VASE (Variable Angle Spectroscopy Ellipsometer of J.A. Woolam Co. Instruments), in a wavelength range between 2 and 4.5 eV. Spectroscopic ellipsometry measurements have been made at different incident angles closed to the film Brewster angle. Acquired data have been simultaneously interpreted with a multilayer dispersion model of the film structure for spectral fitting. This theoretical model assumes an ambient/roughness/film/substrate structure. The surface roughness layer has been modeled using the Bruggeman effective-medium-approximation (EMA) model [23] by assuming a mixture between the top layer in the model and the ambient material (air for us). To model the film layer we started from a collection of oscillator functions that compose a generic Zinc-Oxide transparent conductive layer in the spectral range 190-1700 nm. The substrates have been previously

investigated and modeled. The fitting procedure uses a non-linear regression method which aims to minimize the root mean square error.

The I-V characteristics of ZnO device have been collected, both in vacuum and in air. The optoelectrical response of the device has been also evaluated, in terms of responsivity and speed of the device, both in air and in vacuum, using an LED operating at 365 nm for the generation of the incident light.

## 2. Results and discussion

### 2.1 Structural and morphological characterization

Crystal structure of ZnO is usually the hexagonal wurtzite type with unit cell constants  $a = 3.24 \text{ \AA}$  and  $c = 5.19 \text{ \AA}$ . In Fig. 1 XRD spectra of an as-grown (black line) and after the annealing process (red line) ZnO film are reported. The structural analysis confirmed a Zn excess in the as-grown films that has been eliminated by the subsequent annealing at high temperature.

The as-grown film was Zn-rich, and the ZnO peaks appeared just after the thermal treatment. The sample showed a polycrystalline nature, with (100), (002) and (101) most intense peaks of hexagonal ZnO at  $37.148^\circ$ ,  $40.228^\circ$  and  $42.457^\circ$ . No preferential orientation is detected.

The average grain size of the films has been calculated using the Scherrer's formula:

$$D = 0.9\lambda/\beta \cos\theta \quad (1)$$

where  $\lambda$ ,  $\beta$  and  $\theta$  are the x-ray wavelength ( $1.789 \text{ \AA}$ ), full width at half maximum (FWHM) of the (101) peak and the Bragg diffraction angle, respectively. The average grain size of the films ranges between 15 and 20 nm, in agreement with results from literature [6].

SEM and AFM studies were used to characterize the surface morphology of the films.

SEM analysis (Fig. 2) showed a granular surface, confirmed by AFM morphological characterization. AFM image with area of  $5 \mu\text{m} \times 5 \mu\text{m}$  of the as-grown sample is reported in Fig. 3.

The sample has a mounded surface constituted of rounded grains grown on columnar pillars. The surface analysis has been performed by the examination of the correlation between the heights of the surface points through the height–height correlation functions  $g(R)$  [24]. The correlation function is a measure of the relative height fluctuation in a rough surface and for real self-affine surfaces has the following behavior [25]:

$$g(R) \propto r^{2\alpha}, R \ll \xi \quad (2)$$

$$g(R) = 2\sigma^2, R \gg \xi \quad (3)$$

where  $R = r' - r$  [ $r = (x, y)$  in-plane positional vector].  $g(R)$  is determined by a small number of parameters: the RMS value  $\sigma$ , describing the vertical development of roughness, the roughness exponent  $\alpha$  and the correlation length  $\xi$ . The calculated parameter  $\alpha$  for the ZnO surface has a value of 0.6. Usually, a large value of  $\alpha$  ( $> 0.5$ ) corresponds to a smooth textured surface structure in a short range, while a smaller value of  $\alpha$  ( $< 0.5$ ) corresponds to a more jagged local surface morphology. Following theoretical prediction of Eq. 3, for large  $R$ , the  $g(R)$  function stabilizes about the  $2\sigma^2$  value: in this case, the RMS value  $\sigma$  of the roughness is about 20 nm, when evaluated from  $5 \text{ by } 5 \mu\text{m}^2$  image and a little bit less (17 nm) when evaluated on smaller areas ( $2 \text{ by } 2 \mu\text{m}^2$ ).

The correlation length  $\xi$  quantifies the density of the surface fluctuations and corresponds to the transition from the power law behavior to the stabilization. It has a value that ranges between 80 nm

(2 by 2  $\mu\text{m}^2$  area) and 110 nm (5 by 5  $\mu\text{m}^2$  area). This is confirmed by the analysis of the particles dimension, that have an average diameter of about 100 nm.

The particle size of ZnO films analyzed by AFM is much greater than that by XRD. This may suggest that AFM gives the particle size, while XRD gives the grain size. Other previous works have reported analogous results and used similar explanation for ZnO and TiO<sub>2</sub> films [26, 27]

## 2.2 Ellipsometry

### 2.2.1 Optical constants

Typical ellipsometric spectra are given in Fig. 4, where the  $(\Psi, \Delta)$  pairs are the measured ellipsometric parameters and refer to the Fresnel's reflection coefficients  $r_s$  and  $r_p$  by the Eq. 4:

$$r_s/r_p = \tan(\Psi)e^{i\Delta} \quad (4)$$

The VASE measurements were performed at room temperature with a spot beam lower than 2 mm in diameter, at incidence angles of 55°, 65° and 70° (the sample Brewster angle was observed around 60°). To acquire high precision data, insensitive to the compensator, polarizer and analyzer azimuth angle errors and imperfections, the ellipsometer was set to average data at two compensator angles  $\pm 45^\circ$ . Since ZnO is transparent in the visible region, ellipsometric data were acquired in the spectral range from 2.50 to 4.55 eV (steps of 0.15 eV) corresponding to the wavelength range 250 nm – 620 nm. The aim is to determine the dielectric complex functions  $(\epsilon_1 + i\epsilon_2)$ , or the optical constants  $(n + ik)$  in alternative, of the material, building a realistic model of the thin film structure. The best fit of the ellipsometric spectra is obtained choosing the model shown in Tab. 1, i.e. a multilayer model that assumes, on sapphire substrate (Al<sub>2</sub>O<sub>3</sub>), a ZnO structure (genosc), a ZnO-type layer (cauchy) and a surface roughness on the top.

The sapphire substrate refractive index was taken as tabulated values from Palik handbook [28]. The ZnO thicker structure was modeled by exploiting the General Oscillator Layer (or “GenOsc



layer”) of Wollam VASE software. This layer allows to choose from a large variety of oscillator models and dispersion equations to compare and fit optical constants starting from a reference material: in this case, a generic Zinc-Oxide transparent conductive layer, available in the analysis software. The real  $\varepsilon_1$  and imaginary  $\varepsilon_2$  part of the complex dielectric function of GenOsc layer are shown in Fig. 5 (left). The Cauchy layer [29] is an empirical model based on the Cauchy function employed to simulate an absorption behavior. The top layer is the surface roughness. It was modeled via the Bruggeman EMA approach assuming a mixture of 50% between the top layer in the model and the air.

Solid lines in Fig. 4 are the best fit of the measured data for the three incidence angles fitted simultaneously with the above model. The layer thicknesses were used as fit parameters to know the goodness of the model, finding an overall structure of 277 nm divided as follows: a thicker zinc-oxide of 158 nm on the substrate, a thinner absorption layer of 115 nm and on the top a 4 nm of roughness. The overall thickness results in agreement with an average value measured by profilometer: 280 nm. Fig. 5 (right) shows the complex dielectric functions of the Cauchy layer calculated “point-by-point” using the fitting model and they result similar to those of GenOsc layer (Fig. 5 (left)), but with higher values for imaginary part  $\varepsilon_2$  (and lower for real values  $\varepsilon_1$ ) that is related to a less transparent material. Hence probably, the annealing processes have modified the top side of the zinc-oxide deposited film, building this layer that maintains a trend similar to the original material, but with a more absorbent behavior. Anyway these complex dielectric functions are in agreement with those of Matz and Luth [30] measured from a bulk sample.

### 2.2.2 Optical absorption band gap

The optical band gap  $E_g$  can be calculated from the Tauc formula [31]  $\alpha h\nu = A(h\nu - E_g)^{1/2}$  where,  $A$  is a constant,  $h\nu$  is the photon energy and  $\alpha$  is the absorption coefficient of the film under test. The absorption coefficient can be derived from the Beer-Lambert law  $\alpha = 4\pi k/\lambda$  where  $k$  is the imaginary part of the refractive index and  $\lambda$  is the wavelength.

Since the optical model of our film (Tab.1) is not a single layer with a well-defined  $k$ , we preferred to calculate the transmittance  $T$  and the reflectance  $R$  of deposited film from the model and rewriting the Beer-Lambert law explicating  $T$  and  $R$  (Eq. 5), which means to consider an equivalent single layer from the absorption point of view:

$$\alpha = (1/d) \ln(1-R)^2/T \quad (5)$$

where  $d$  is the sample thickness (277 nm). Fig. 6 shows the Tauc plot: the square of the absorption coefficient ( $\alpha h\nu$ ) as a function of the photon energy ( $h\nu$ ). From this plot it is possible to obtain the energy band gap  $E_g = 3.20$  eV. Similar values are obtained in [2] where is shown how  $E_g$  changes as a function of the annealing temperature in a film of 500 nm thick.

### 3.2 UV detector characterization

Fig. 7 shows the dark (circles) and photo-illuminated (squares) current-voltage (I-V) characteristics of the ZnO detector in vacuum, where the rectifying behavior of the interdigitated Al contacts is clearly visible. This is induced by the oxidation step in  $H_2O_2$  that, according to literature [22, 32], should remove the conductive  $-OH$  layer and make the ZnO-Al a Schottky junction. This is also confirmed by the increasing of 3 order of magnitude of the resistivity of the ZnO films measured using a 4-points probe in air before and after the oxidation process.

The maximum photo-current gain  $[(I_{UV} - I_{dark})/I_{dark}]$  of the device is about 9, which is a considerable values if compared with data in literature [3]. The responsivity under exposure to UV light (365 nm) has been calculated to be 15 A/W at 10 V of bias and no measurable response has been detected in the visible spectral range. Therefore, the ZnO sensors device acts as a photoconductor which is sensitive only in the UV region. The time dependent photo-response of the device upon UV illumination at room temperature in vacuum in illustrated in Fig. 8. The photo-response, due to

1 a UV pulse irradiation, follows an exponential growth and decay trend. The photo-current rises  
2 exponentially upon UV illumination following the two-phase exponential association function  
3  
4

$$5 \quad I = k + I_{01} (1 - e^{-t/\tau_1}) + I_{02}(1 - e^{-t/\tau_2}) \quad (6)$$

6  
7  
8

9 according to other data in literature [2]. Turning off the UV ray, the photo-current decreases  
10 following the second-order exponential decay (Eq. 6) and both rising and decay time constants have  
11 been estimated to be 29 s.  
12  
13  
14  
15

#### 16 17 18 **4. Conclusions** 19 20

21 ZnO thin films fabricated on sapphire by electron gun and a two-steps ex-situ treatment are  
22 polycrystalline and with a smooth surface and show very good visible transparency and energy gap  
23 of 3.2 eV. The Al interdigitated contacts show a Schottky behavior, which is strongly desired in  
24 perspective of application since it has many advantages in the aspects of high quantum efficiency  
25 response speed, low dark current, high UV/visible contrast and possible zero-bias operation. The  
26 fabricated detector shows a responsivity of 15 A/W at 10 V. The next goal is the achievement of the  
27 same performance in air, by a more robust oxidation step in hydrogen peroxide or in plasma, in  
28 order to passivate the surface of the samples thus limiting the chemisorption phenomena.  
29  
30  
31  
32  
33  
34  
35  
36  
37  
38  
39  
40

#### 41 42 **Acknowledgements** 43 44

45 The work leading to this study was partly funded by the EMRP ENV03 Project "Traceability for  
46 surface spectral solar ultraviolet radiation". The EMRP is jointly funded by the EMRP participating  
47 countries within EURAMET and the European Union.  
48  
49  
50  
51  
52  
53  
54  
55  
56  
57  
58  
59  
60

#### 61 62 **References** 63 64 65

- [1] C. Jagadish and S. J. Pearton, Zinc Oxide Bulk, Thin Films and nanostructures, 1<sup>st</sup> ed., Elsevier Science, 2006.
- [2] E. Monroy, F. Omnes, F. Calle, Semicond. Sci. Technol. **18** R33 (2003).
- [3] S.K. Panda, C. Jacob, Solid-State Electronics **73** 44 (2012).
- [4] S.J. Chen, Y.C. Liu, G. Ma, D.X. Zhao, Z.Z. Zhi, Y.M. Lu, J.Y. Zhang, D.Z. Shen, X.W. Fan, J. Cryst. Growth **240** 467 (2002).
- [5] Y. Chen, D. M. Bagnall, H. Koh, K. Park, K. Hiraga, Z. Zhu, Takafumi Yao, J. Appl. Phys. **84** 3912 (1998).
- [6] S.J. Young, L.W. Ji, S.J. Chang, Y.K. Su, J. Cryst. Growth **293** 43-47 (2006).
- [7] M. Li, W. Anderson, N. Chokshi, R. L. DeLeon, Gary Tompa, J. Appl. Phys. **100** 053106 (2006).
- [8] Y.W. Heo, K. Ip, S.J. Pearton , D.P. Norton, J.D. Budai, Appl. Surf. Sci. **252** 7442 (2006).
- [9] Sheng Chu, M. Morshed, L. Li, J. Huan, J. Liu, J. Cryst. Growth **325** 36 (2011).
- [10] F. Vigue' , P. Vennéguès , C. Deparis, S. Vézian, M. Laügt, J.-P. Faurie, J. Appl. Phys. **90** 5115 (2001).
- [11] K. Saravanakumar, V. Ganesan, N.P. Lalla, C. Gopinathan, K. Mahalakshmi, C. Sanjeeviraja, Adv. Stud. Theor. Phys. **5** 143 (2011).
- [12] S. Bensmaine, L. Le Brizoual, O. Elmazria, B. Assouar, B. Benyoucef, J. Electron. Devices **5** 104 (2007).
- [13] X.M. Fan, J.S. Lian, Z.X. Guo, H.J. Lu, Appl. Surf. Sci. **239** 176 (2005).

- [14] B.J. Jin, S. Im, S.Y. Lee, Thin Solid Films **366** 107 (2000).
- [15] N. Lehraki, M.S. Aida, S. Abed, N. Attaf, A. Attaf, M. Poulain, Curr. Appl. Phys. **12** 1283 (2012).
- [16] R. Ayouchi, F. Martin, D. Leinen, J.R. Ramos-Barrado, J. Cryst. Growth **247** 497 (2003).
- [17] Junjie Zhu, In-Hwan Lee, Ran Yao, Zhuxi Fu, J. Korean Phys. Soc. **50** 598 (2007).
- [18] Lamia Znaidi, Mater. Sci. Eng. B **174** 18 (2010).
- [19] K.Y. Tse, H.H. Hnga, S.P. Lau, Y.G. Wang, S.F. Yu, Ceram. Int. **30** 1669 (2004).
- [20] D. C. Agarwal, R. S. Chauhan, A. Kumar, D. Kabiraj, F. Singh, S. A. Khan, D. K. Avasthi, J. C. Pivin, M. Kumar, J. Ghatak, P. V. Satyam, J. Appl. Phys. **99** 123105 (2006).
- [21] M. Liu, H.K. Kim, Appl. Phys. Lett. **84** 173 (2004).
- [22] Q. L. Gu, C. C. Ling, X. D. Chen, C. K. Cheng, A. M. Ng, C. D. Beling, S. Fung, A. B. Djuricic, L. W. Lu, Appl. Phys. Lett. **90** 122101 (2007).
- [23] D.A.G. Bruggeman, Ann. Phys. **24** 636 (1935).
- [24] G. Palasantzas, Phys. Rev. B **48** 14472 (1993).
- [25] H.N. Yang, G.C. Wang, T. M. Lu, Diffraction From Rough Surfaces and Dynamic Growth Fronts, World Scientific, 1993.
- [26] Z. B. Fang, Z. J. Yana, Y.S. Tan, X.Q. Liu, Y.Y. Wang, Appl. Surf. Sci. **241** 303 (2005).
- [27] G. Wei, Y.J. Zhang, R.C. Xiong, Sci. Chin. (Series B) **46** 184 (2003).
- [28] Edward D. Palik, Handbook of Optical Constants of Solids, Elsevier, 1998, Vol 2 pp. 769.

[29] H.G. Tompkins and W.A. McGahan, Spectroscopy Ellipsometry and Reflectometry, J. Wiley & Sons Inc., New York, 1999.

[30] R. Matz and H.Luth, Appl. Phys.**18** 1123 (1979).

[31] J.Tauc, Optical properties of solids, Amsteden, North-Hollande, 1972.

[32] B. Angadi, H. C. Park, H. W. Choi, J. W. Choi, W. K. Choi, J. Phys. D: Appl. Phys. **40** 1422 (2007).

Figure 1  
[Click here to download high resolution image](#)

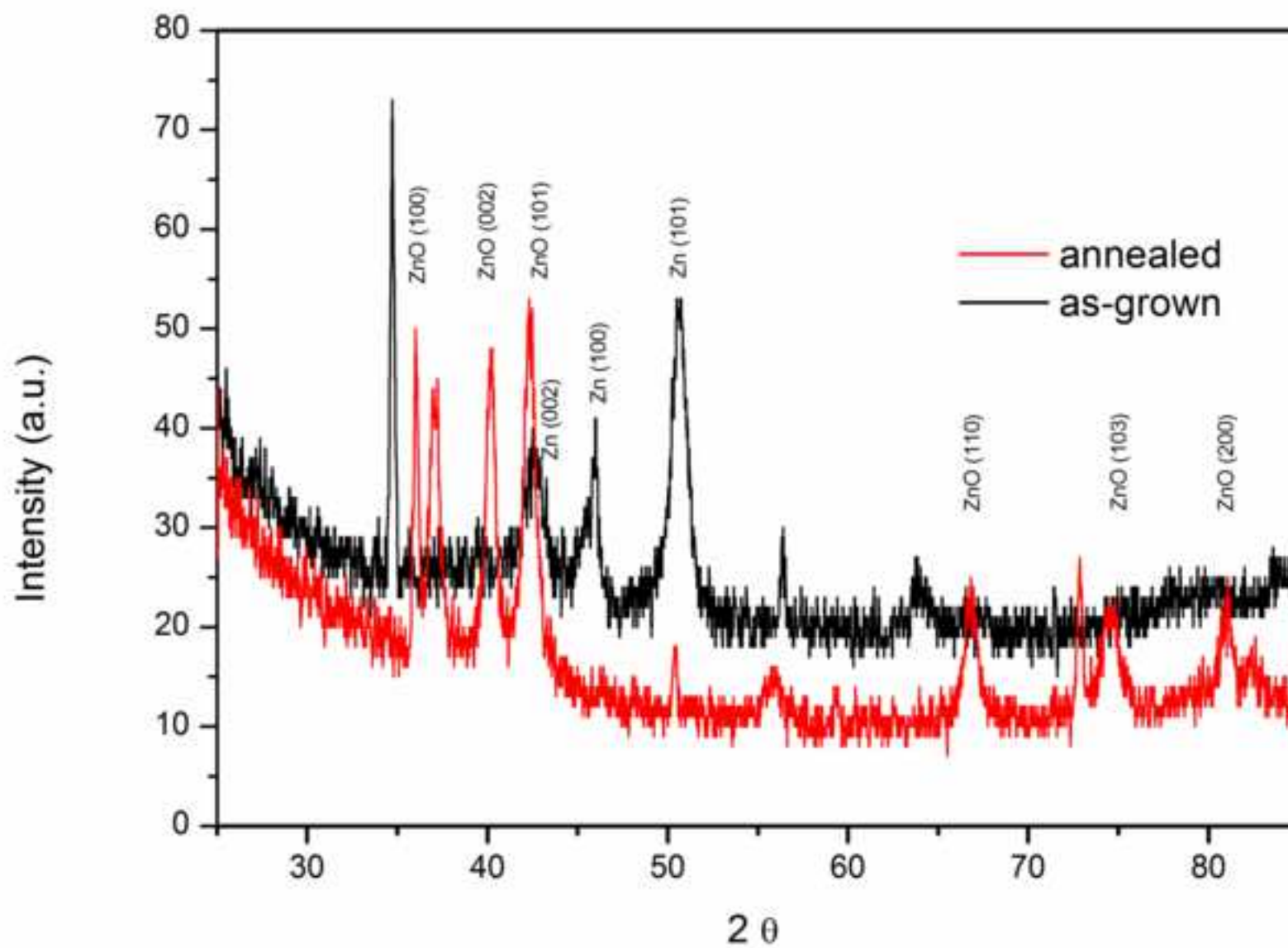


Figure 2

[Click here to download high resolution image](#)

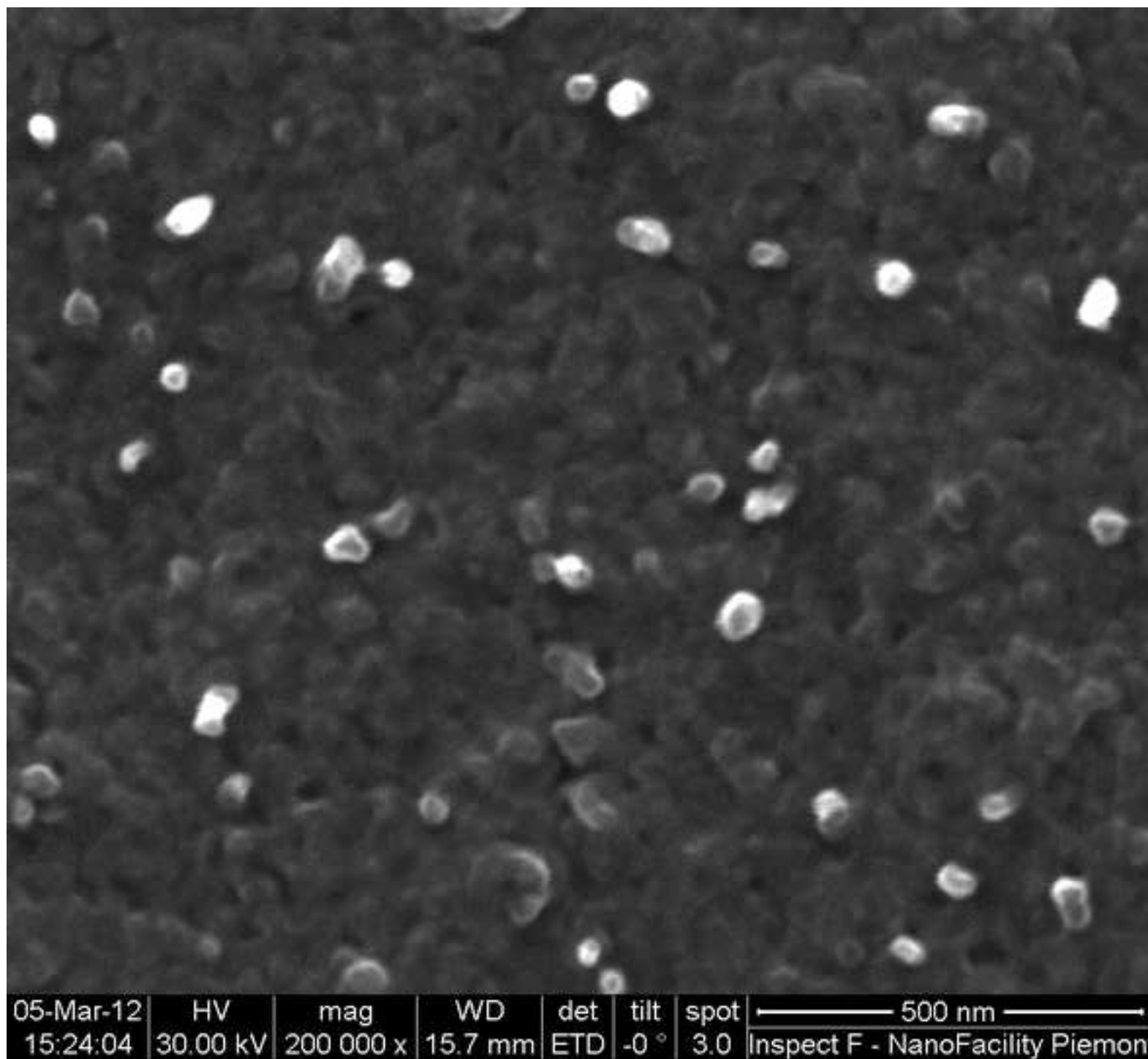




Figure 3  
[Click here to download high resolution image](#)

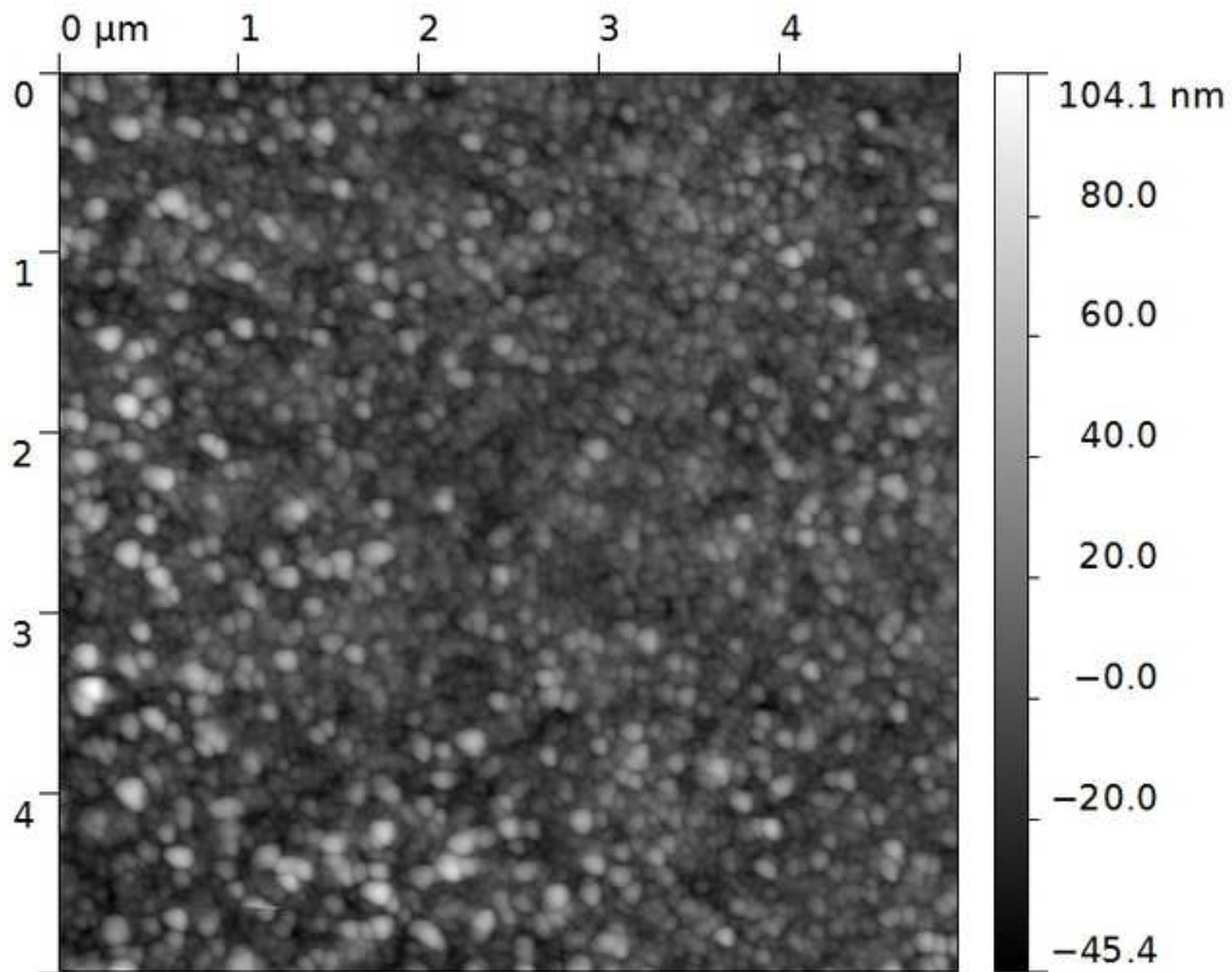


Figure 4  
[Click here to download high resolution image](#)

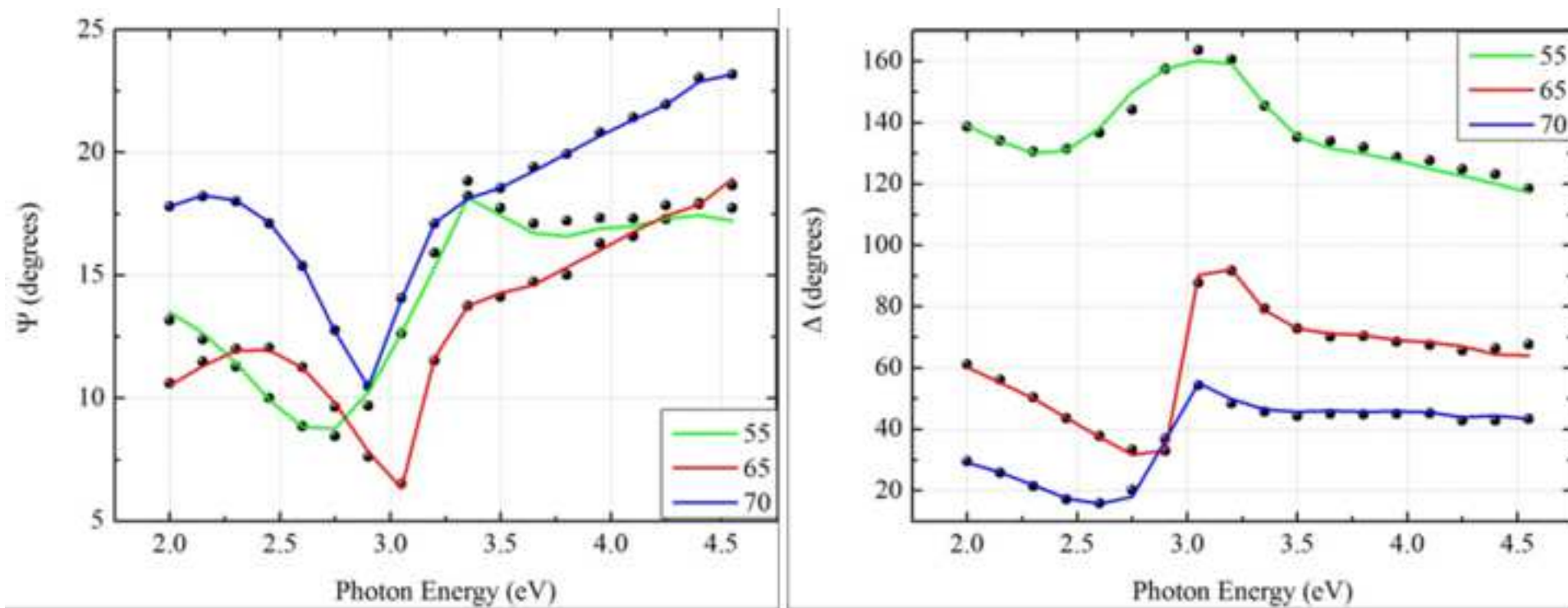


Figure 5  
[Click here to download high resolution image](#)

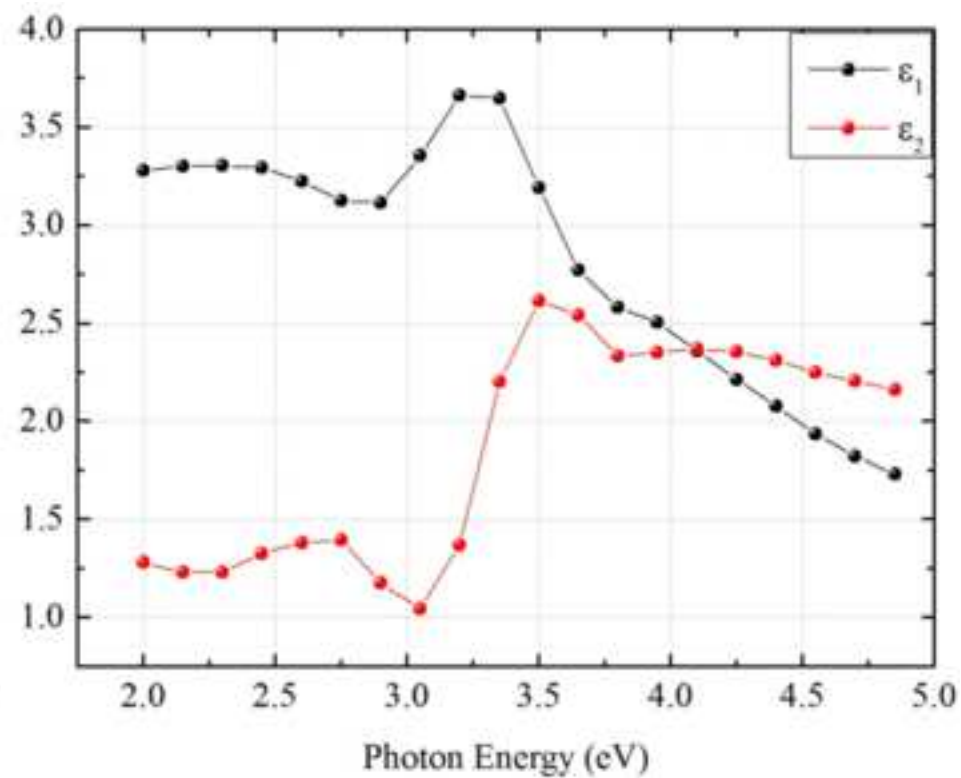
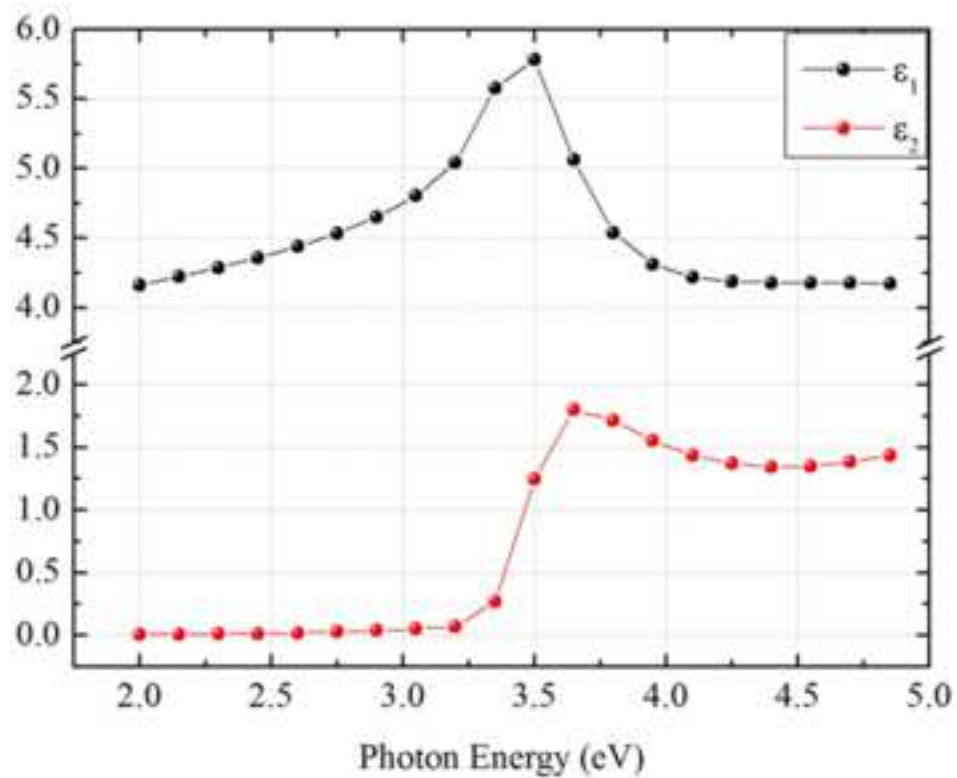


Figure 6  
[Click here to download high resolution image](#)

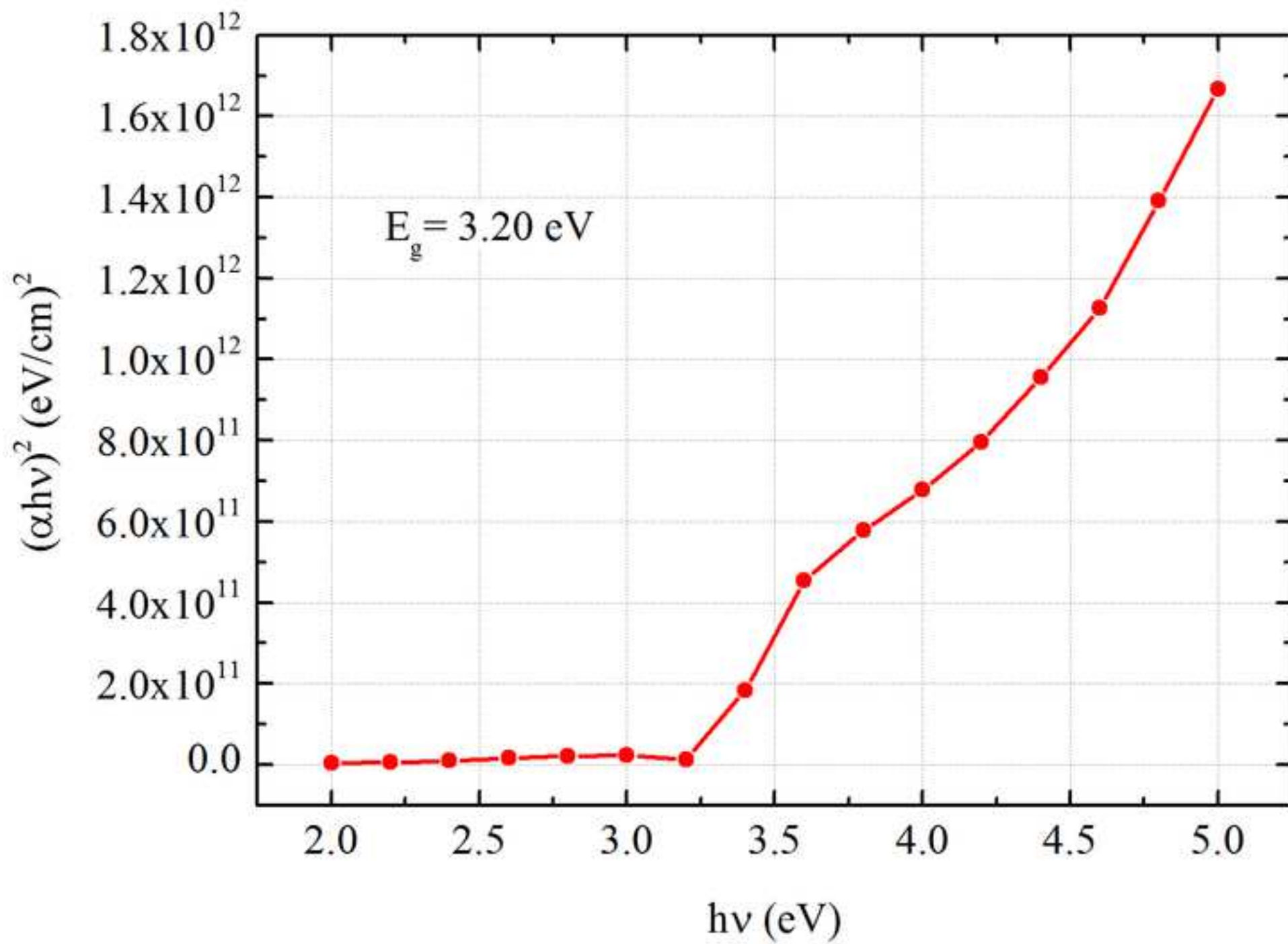


Figure 7  
[Click here to download high resolution image](#)

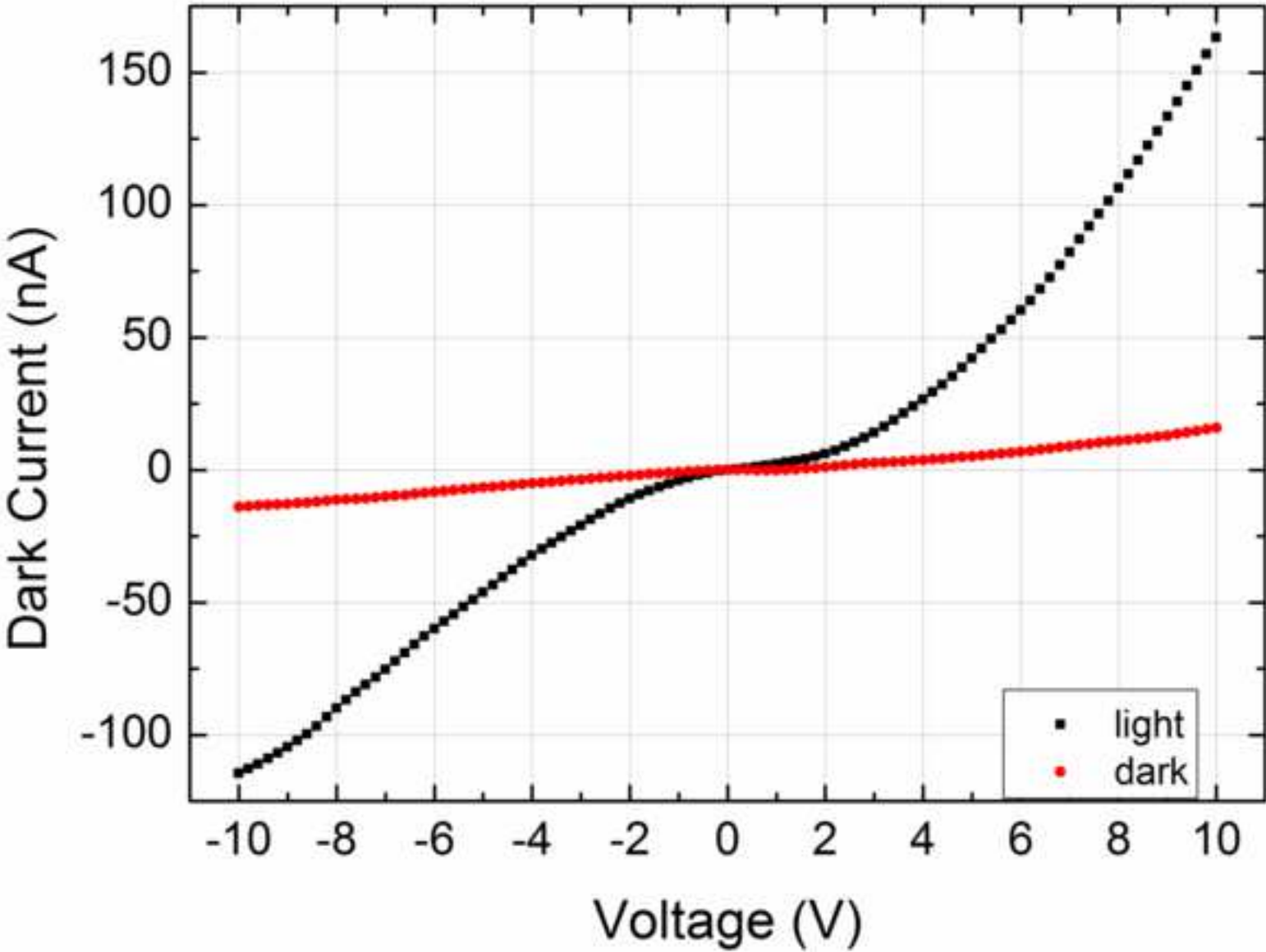
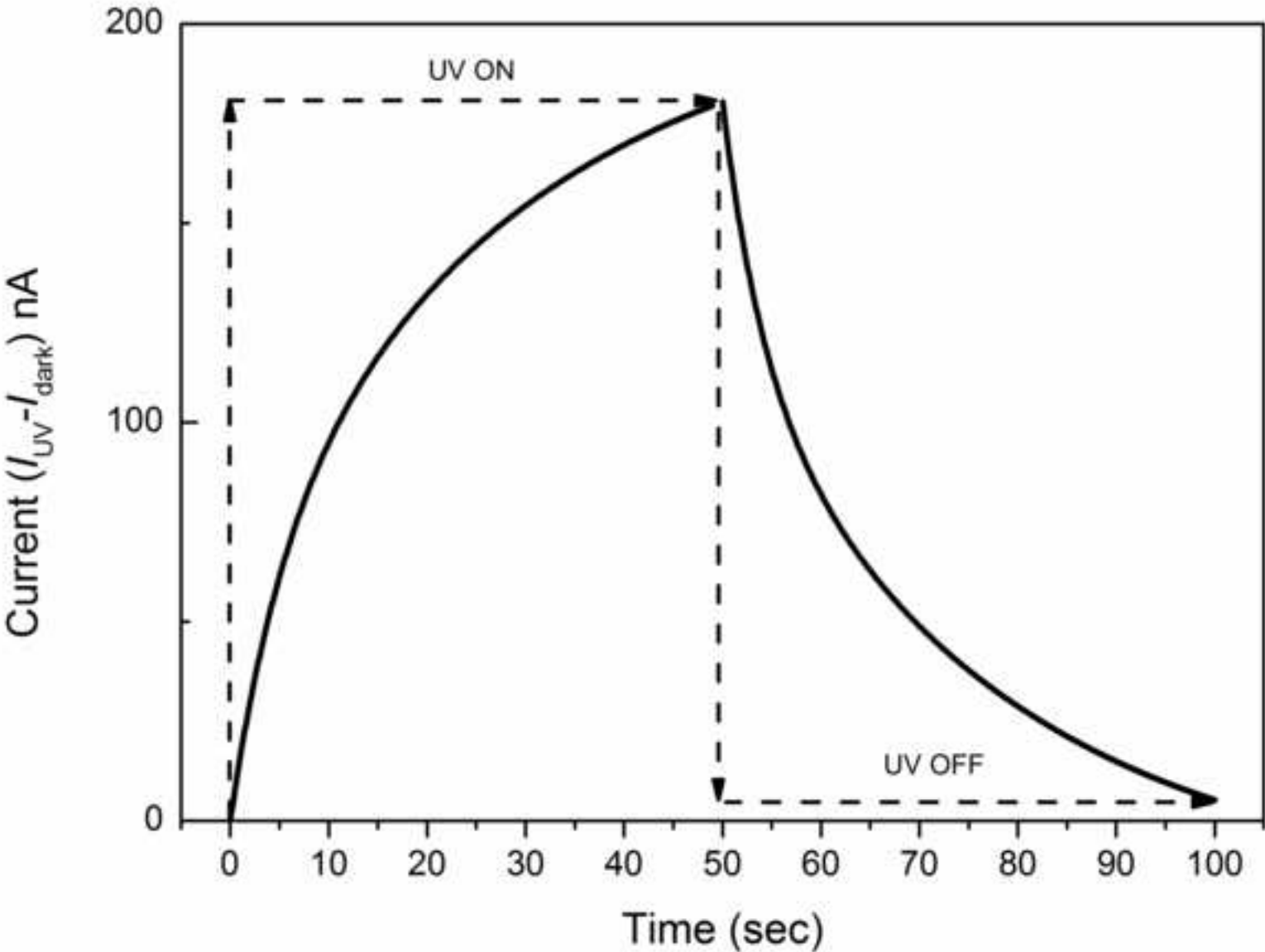


Figure 8  
[Click here to download high resolution image](#)



Table

[Click here to download high resolution image](#)

